

An efficient numerical algorithm for the inversion of an integral transform arising in ultrasound imaging

Souvik Roy* · Venkateswaran P.
Krishnan* · Praveen Chandrasekhar* ·
A. S. Vasudeva Murthy*

Received: date / Accepted: date

Abstract We present an efficient and novel numerical algorithm for inversion of transforms arising in imaging modalities such as ultrasound imaging, thermoacoustic and photoacoustic tomography, intravascular imaging, non-destructive testing, and radar imaging with circular acquisition geometry. Our algorithm is based on recently discovered explicit inversion formulas for circular and elliptical Radon transforms with radially partial data derived by Ambartsoumian, Gouia-Zarrad, Lewis and by Ambartsoumian and Krishnan. These inversion formulas hold when the support of the function lies on the inside (relevant in ultrasound imaging, thermoacoustic and photoacoustic tomography, non-destructive testing), outside (relevant in intravascular imaging), both inside and outside (relevant in radar imaging) of the acquisition circle. Given the importance of such inversion formulas in several new and emerging imaging modalities, an efficient numerical inversion algorithm is of tremendous topical interest. The novelty of our non-iterative numerical inversion approach is that the entire scheme can be pre-processed and used repeatedly in image reconstruction, leading to a very fast algorithm. Several numerical simulations are presented showing the robustness of our algorithm.

Keywords Circular Radon transform, elliptical Radon transform, Volterra integral equations, Truncated singular value decomposition, Thermoacoustic tomography, Photoacoustic tomography, Ultrasound reflectivity imaging, Intravascular imaging, Radar imaging

*TIFR Centre for Applicable Mathematics, Bangalore, India
Tel.: +91-80-66953790
Fax: +91-80-66953799
E-mail: souvik,vkrishnan,praveen,vasu@math.tifrbng.res.in

1 Introduction

In several imaging modalities such as ultrasound reflectivity imaging, thermoacoustic and photo-acoustic tomography, intravascular imaging, non-destructive testing and radar imaging, circular or elliptical Radon transforms arise naturally. These are transforms that associate to a function, its integrals along a family of circles or ellipses.

In ultrasound imaging, ultrasonic pulses emitted from a transducer moving along a curve (typically a circle), propagate inside the medium and reflect off inhomogeneities which are measured by the same or a different moving transducer. Assuming that the speed of sound propagation within the medium is constant and that the medium is weakly reflecting, the pulses registered at the receiver transducer is the superposition of all the pulses reflected from those inhomogeneities such that the total distance traveled by the reflected pulse is a constant. This leads to the consideration of an integral transform of a function on a plane (which models the image to be reconstructed), given its integrals along a family of circles (for the case of identical emitter/receiver) or ellipses (for spatially separated emitter/receiver). The goal is to recover an image of the medium given these integrals. In other words, one is interested in the inversion of a circular or elliptical Radon transform. For a detailed discussion of the mathematical model of ultrasound imaging, we refer the reader to [25–27]. Similarly, the mathematical formulation of problems in thermoacoustic and photoacoustic tomography, non-destructive testing, intravascular imaging, radar and sonar imaging all lead to inversion of circular or elliptical Radon transforms. For details, we refer the reader to the following references [23, 8, 4].

The inversion of circular Radon transforms has been extensively studied by several authors [1, 2, 7, 31, 32, 13, 9, 12, 15, 14, 16, 37, 29, 10, 30], and to a lesser extent, that of elliptical Radon transforms [24, 36, 39, 3, 28, 17]. All these papers deal with full data in the radial direction. In some imaging problems, full data in the radial direction is not available, as is the case of imaging the surrounding region of a bone. To this end, Ambartsoumian, Gouia-Zarrad and Lewis in [5] found an explicit inversion formulas for the circular Radon transform with circular acquisition geometry (one of the most widely used ways of collecting data) when half of the data in the radial variable is available. These results were recently generalized by Ambartsoumian and Krishnan for a class of elliptical and circular Radon transforms in [6]. The inversion formulas in these papers are given for three cases: support of the function is inside, outside and on both sides of the acquisition circle. The case when the support is inside the circle of acquisition is of importance in ultrasound reflectivity imaging, thermoacoustic and photoacoustic tomography, and non-destructive testing. When the support is outside and on both sides of the acquisition circle, the inversion formulas are applicable in intravascular and radar imaging, respectively. Given the importance of these inversion formulas in several imaging modalities, efficient numerical inversion is of great interest. The main contribution of this paper is a novel implementation of the inversion formulas for

a class of circular and elliptical Radon transforms with radially partial data obtained in these papers.

The inversion formulas given in [5,6] were based on an inversion strategy due to Cormack [11] that involved Fourier series techniques. As shown in these papers, the n^{th} Fourier coefficient of the circular (elliptical) Radon transform data is related to the n^{th} Fourier coefficient of the unknown function by a Volterra-type integral equation of the first kind with a weakly singular kernel. This can be transformed to a Volterra-type integral equation of the second kind in which the singularity is removed [38]. It is well known that such an integral equation has a unique solution and this can be obtained by the Picard's process of successive approximations, leading to an exact inversion formula given by a infinite series of iterated kernels; see [38].

In this paper, we numerically invert Volterra-type integral equation of the first kind adopting a numerical method given in [41] (see also [33]) and combine it with a truncated singular value decomposition to recover the Fourier coefficients of the unknown function from the circular or elliptical Radon transform data. The same method can also be implemented for numerical inversion of Volterra-type integral equation of the second kind proved in the papers [5, 6], but the numerical inversion is less accurate (see Remark 1). The numerical implementation of the exact inversion formula for the Volterra integral equation of the second kind involving an infinite series of iterated kernels is very unstable and implementing them is still an open problem. To the best of our knowledge, ours is the first successful numerical inversion of circular and elliptical Radon transforms for the circular geometry of acquisition with radially partial data, the theoretical results of which, as already mentioned, were presented in [5] and [6].

This paper is organized as follows. §2 gives the relevant theoretical background recalling the inversion formulas for the circular and elliptical Radon transforms based on which the numerical simulations in this paper are performed. §3 gives the numerical algorithm for inverting a Volterra-type integral equation of first kind and second kind. In §4, we present the numerical simulations, and §5 summarizes the results obtained.

2 Theoretical background

As mentioned in the introduction, we consider two generalized Radon transforms in the plane: (a) Circular Radon transform and (b) Elliptical Radon transform.

Circular Radon transform

Let $\partial B(0, R)$ denote the circle of radius R centered at $(0, 0)$ and parametrized by

$$\gamma(\phi) = (R \cos \phi, R \sin \phi) : \phi \in [0, 2\pi].$$

Let $\rho > 0$ and define the circle of radius ρ centered at $\gamma(\phi)$:

$$C(\rho, \phi) = \{x \in \mathbb{R}^2 : |x - \gamma(\phi)| = \rho\}$$

Let (r, θ) denote the standard polar coordinates on the plane and let $f(r, \theta)$ be a compactly supported function in \mathbb{R}^2 . The circular Radon transform of f over the circle $C(\rho, \phi)$ is defined as

$$g^C(\rho, \phi) = R^C f(\rho, \phi) = \int_{C(\rho, \phi)} f(r, \theta) ds.$$

Here ds is the arc-length parametrization on the circle $C(\rho, \phi)$. See Figure 1a.

Elliptical Radon transform

We consider $\partial B(0, R)$ as before and let $\alpha \in (0, \pi/2)$ be a fixed angle. The ellipses of interest to us are the ones with their foci on $\partial B(0, R)$ separated by the polar angle 2α . Define $a = R \sin \alpha$ and $b = R \cos \alpha$. Given (ρ, ϕ) , we consider the foci locations to be $\gamma_{f_1}(\phi) = (R \cos(\phi - \alpha), R \sin(\phi - \alpha))$ and $\gamma_{f_2}(\phi) = (R \cos(\phi + \alpha), R \sin(\phi + \alpha))$. Now consider the ellipse

$$E(\rho, \phi) = \{x \in \mathbb{R}^2 : |x - \gamma_{f_1}(\phi)| + |x - \gamma_{f_2}(\phi)| = 2\sqrt{\rho^2 + a^2}\}.$$

The elliptical Radon transform of f over $E(\rho, \phi)$ is defined as

$$g^E(\rho, \phi) = R^E f(\rho, \phi) = \int_{E(\rho, \phi)} f(r, \theta) ds,$$

where ds is the arc-length parametrization on $E(\rho, \phi)$. See Figure 1b.

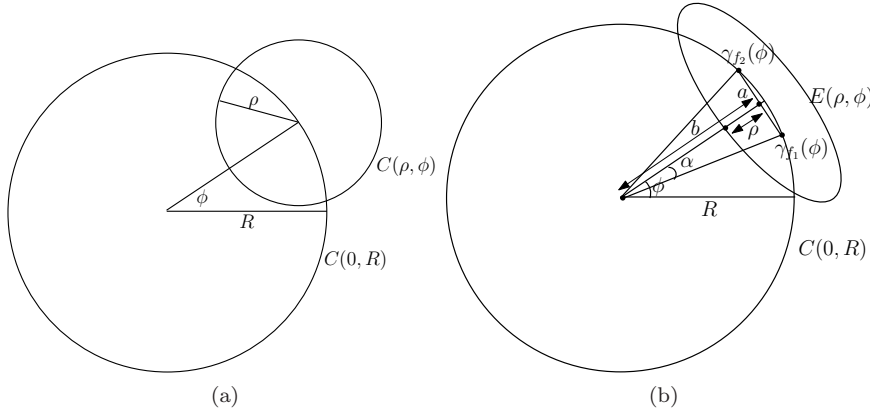


Fig. 1: Circular and elliptical Radon transform set-up

The transforms R^C and R^E with radially partial data were considered in [5,6] and explicit inversion formulas were given there. The inversion of these transforms leads to the inversion of a Volterra-type integral equation of the first kind with a weakly singular kernel. This in turn is transformed to an integral equation of the second kind with the singularity removed and the inversion of such an integral equation is given as an infinite series involving iterated kernels. Since we perform numerical inversion of Volterra-type integral equations of the first kind here, in each of the set up below, we only recall the corresponding integral equations of the first kind derived in [5,6] instead of the explicit inversion formulas given as an infinite series.

We expand $f(r, \theta)$, $g^C(\rho, \phi)$ and $g^E(\rho, \phi)$ into a Fourier series:

$$f(r, \theta) = \sum_{n=-\infty}^{\infty} f_n(r) e^{in\theta}, g^C(\rho, \phi) = \sum_{n=-\infty}^{\infty} g_n^C(\rho) e^{in\phi}, g^E(\rho, \phi) = \sum_{n=-\infty}^{\infty} g_n^E(\rho) e^{in\phi}$$

In the following results, f_n is related to g_n^C or g_n^E through a Volterra-type integral equation of the first kind. We will use the superscripts *Int*, *Ext* or *Both* to denote the cases when the support of the function is an annular region in the interior, exterior or on both sides of the circle $\partial B(0, R)$, respectively.

Theorem 1 (Functions supported in an annulus interior to $\partial B(0, R)$)
[5, 6]

1. [5, Thm. 1](Circular transform) Let $0 < \epsilon < R$ and $f(r, \theta)$ in polar coordinates be an unknown continuous function supported inside the annular region $A(\epsilon, R) = \{(r, \theta) : r \in (\epsilon, R), \theta \in [0, 2\pi]\}$. If $R^C f(\rho, \phi)$ is known for $\phi \in [0, 2\pi]$ and $\rho \in [0, R - \epsilon]$, then $f(r, \theta)$ can be uniquely recovered in $A(\epsilon, R)$.
2. [6, Thm. 3.1](Elliptical transform) Let $f(r, \theta)$ be a continuous function supported inside the annulus $A(\epsilon, b)$. Suppose $R^E f(\rho, \phi)$ is known for all $\phi \in [0, 2\pi]$ and $\rho \in (0, b - \epsilon)$, then $f(r, \theta)$ can be uniquely recovered.

The proof of the above theorem is based on the inversion of Volterra-type integral equations of the first kind (1) and (3). Here $g_n^{C, \text{Int}}$ and $g_n^{E, \text{Int}}$ are the n^{th} Fourier coefficients of the circular and elliptical Radon transform data $R^C f(\rho, \phi)$ and $R^E f(\rho, \phi)$, respectively.

1. Circular case, see [5]

$$g_n^{C, \text{Int}}(\rho) = \int_0^\rho \frac{K_n(\rho, u) F_n(u)}{\sqrt{\rho - u}} du, \quad (1)$$

where

$$\begin{aligned} F_n(u) &= f_n(R - u), & T_n(x) &= \cos(n \arccos(x)) \\ K_n(\rho, u) &= \frac{4\rho(R - u)T_n\left[\frac{(R-u)^2 + R^2 - \rho^2}{2R(R-u)}\right]}{\sqrt{(u + \rho)(2R + \rho - u)(2R - \rho - u)}}. \end{aligned} \quad (2)$$

2. Elliptical case, see [6]

$$g_n^{\text{E,Int}}(\rho) = \int_0^\rho \frac{K_n(\rho, u)F_n(u)}{\sqrt{\rho-u}} du, \quad (3)$$

where

$$F_n(u) = f_n(b-u)$$

$$K_n(\rho, u) = \frac{\tilde{K}_n(\rho, b-u)\sqrt{\rho-u}}{\sqrt{a^2 + b\rho - \sqrt{R^2\rho^2 + a^2(R^2 - (b-u)^2)}}} \quad (4)$$

$$\tilde{K}_n(\rho, r) = \frac{2arT_n \left(\frac{b(\rho^2+a^2) - \rho\sqrt{R^2\rho^2+a^2(R^2-r^2)}}{a^2r} \right)}{\sqrt{a^2 + (\sqrt{R^2\rho^2 + a^2(R^2 - r^2)} - b\rho)}} \times$$

$$\frac{\sqrt{2R^2\rho^2 + a^2(R^2 - r^2) - 2b\rho\sqrt{R^2\rho^2 + a^2(R^2 - r^2)}}}{\sqrt{R^2\rho^2 + a^2(R^2 - r^2)}}. \quad (5)$$

Theorem 2 (Functions supported in an annulus exterior to $\partial B(0, R)$)
[5, Thm. 6]

(Circular transform) Let $f(r, \theta)$ be a continuous function supported inside the annulus centered at 0: $A(R, 3R) = \{(r, \theta) : r \in (R, 3R), \theta \in [0, 2\pi]\}$. If $R^C f(\rho, \phi)$ is known for $\phi \in [0, 2\pi]$ and $\rho \in [0, R_1]$, where $0 < R_1 < 2R$ then $f(r, \theta)$ can be uniquely recovered in $A(R, R_1)$.

The above theorem is proved by inverting the following relation between the n^{th} Fourier coefficient of the circular Radon transform, $g_n^{\text{C,Ext}}$, and the n^{th} Fourier coefficient of the function f derived in [5]

$$g_n^{\text{C,Ext}}(\rho) = \int_0^\rho \frac{K_n(\rho, u)F_n(u)}{\sqrt{\rho-u}} du, \quad (6)$$

where

$$F_n(u) = f_n(R+u)$$

$$K_n(\rho, u) = \frac{4\rho(R+u)T_n \left[\frac{(R+u)^2 + R^2 - \rho^2}{2R(R+u)} \right]}{\sqrt{(u+\rho)(2R+\rho+u)(2R+u-\rho)}}. \quad (7)$$

Theorem 3 (Functions with support on both sides of $\partial B(0, R)$) [6]

- [6, Thm. 3.3](Circular transform) Let $f(r, \theta)$ be a continuous function supported inside the disc $D(0, R_2)$ with $R_2 > 2R$. Suppose $R^C(\rho, \phi)$ is known for all $\phi \in [0, 2\pi]$ and $\rho \in [R_2 - R, R_2 + R]$, then $f(r, \theta)$ can be uniquely recovered in the annulus $A(R_1, R_2)$ where $R_1 = R_2 - 2R$.

2. [6, Thm. 3.4](Elliptical Radon transform) Let $f(r, \theta)$ be a continuous function supported inside the disc $D(0, R_2)$ with $R_2 > 2b$. Suppose $R^E(\rho, \phi)$ is known for all $\phi \in [0, 2\pi]$ and $\rho \in [R_2 - b, R_2 + b]$, then $f(r, \theta)$ can be uniquely recovered in $A(R_1, R_2)$ where $R_1 = R_2 - 2b$.

As with the earlier two results, this theorem is also proved by inverting the following integral transforms relating the n^{th} Fourier coefficient of the function f and the n^{th} Fourier coefficient of the circular Radon transform $g_n^{\text{C,Both}}$ and the elliptical Radon transform $g_n^{\text{E,Both}}$.

1. Circular case, see [6]

$$g_n^{\text{C,Both}}(R_2 + R - \rho) = \int_0^\rho \frac{K_n(\rho, u) F_n(u)}{\sqrt{\rho - u}} du, \quad (8)$$

where

$$F_n(u) = f_n(R_2 - u)$$

$$K_n(\rho, u) = \frac{4(R_2 + R - \rho)(R_2 - u) T_n \left(\frac{(R_2 - u)^2 + R^2 - (R_2 + R - \rho)^2}{2(R_2 - u)R} \right)}{\sqrt{(\rho - u)(2R_2 - \rho - u)(2R + u - \rho)(2R + 2R_2 - \rho - u)}}. \quad (9)$$

2. Elliptical case, see [6]

$$g_n^{\text{E,Both}}(R_2 + b - \rho) = \int_0^\rho \frac{K_n(\rho, u) F_n(u)}{\sqrt{\rho - u}} du, \quad (10)$$

where

$$F_n(u) = f_n(R_2 - u)$$

$$K_n(\rho, u) = \frac{\tilde{K}_n(R_2 + b - \rho, R_2 - u) \sqrt{\rho - u}}{\sqrt{a^2 + b(R_2 + b - \rho) - \sqrt{R^2(R_2 + b - \rho)^2 + a^2(R^2 - (R_2 - u)^2)}}} \quad (11)$$

$$\tilde{K}_n(\rho, r) = \frac{2ar T_n \left(\frac{b(\rho^2 + a^2) - \rho \sqrt{R^2 \rho^2 + a^2(R^2 - r^2)}}{a^2 r} \right)}{\sqrt{a^2 + (\sqrt{R^2 \rho^2 + a^2(R^2 - r^2)} - b\rho)}} \times$$

$$\frac{\sqrt{2R^2 \rho^2 + a^2(R^2 - r^2) - 2b\rho \sqrt{R^2 \rho^2 + a^2(R^2 - r^2)}}}{\sqrt{R^2 \rho^2 + a^2(R^2 - r^2)}}. \quad (12)$$

3 Numerical Algorithm

In this section, we describe the numerical scheme used to invert the integral equations listed in the previous section.

3.1 Fourier coefficients of the circular and elliptical Radon data in the angular variable

Since the functions are real, for reasons of computational efficiency, we compute the modified discrete fast Fourier transform (FFT) of $g^C(\rho, \phi)$ in ϕ for a fixed $\rho \in [\varepsilon, 1 - \varepsilon]$ as follows [34]. The procedure for g^E is very similar.

1. Let N be even and $\{\phi_1, \phi_2, \dots, \phi_N\}$ be a discretization of ϕ . We break the array $g^C(\rho, \phi_k)$ for $1 \leq k \leq N$ into two equal length arrays, A for the odd numbered k and B for the even numbered k . In other words, we let $A = \{g^C(\rho, \phi_{2j-1})\}$ and $B = \{g^C(\rho, \phi_{2j})\}$ for $j = 1, 2, \dots, N/2$.
2. We then create a complex array $h_\rho^c(j) = A(j) + iB(j)$, $j = 1, 2, \dots, N/2$.
3. Next we perform a discrete FFT on h_ρ^c to get $\widehat{h}_\rho^c(n)$, $n = 1, 2, \dots, N/2$.
4. The Fourier series of g^C in the ϕ variable is then given by

$$g_n^C(\rho) = \begin{cases} \frac{1}{2} \left\{ \left(\widehat{h}_\rho^c(n) + \overline{\widehat{h}_\rho^c(\frac{N}{2} - n + 2)} \right) \right. \\ \left. -i \left(\widehat{h}_\rho^c(n) - \overline{\widehat{h}_\rho^c(\frac{N}{2} - n + 2)} \right) \cdot e^{\frac{2\pi i(n-1)}{N}} \right\}, \text{ for } n = 1, \dots, \frac{N}{2} + 1 \\ \widehat{h}_\rho^c(N - n + 2), n = \frac{N}{2} + 2, \dots, N. \end{cases}$$

3.2 Trapezoidal product integration method [41]

The next step is to solve the integral equation of the form

$$g_n(\rho) = \int_0^\rho \frac{F_n(u)K_n(\rho, u)}{\sqrt{\rho - u}} du, \quad (13)$$

Under some assumptions on the kernel K_n and the function g_n , it is known that the integral equation (13) has a unique continuous solution F_n .

Theorem 4 (Existence and uniqueness of solution) [40] *The integral equation (13) has a unique continuous solution $F_n(u)$ for $u \in [0, R]$ under the following assumptions:*

1. *The functions*

$$K_n(\rho, u) \text{ and } \frac{\partial}{\partial \rho} K_n(\rho, u)$$

are continuous $0 \leq u \leq \rho \leq R$,

2. *$K_n(\rho, \rho) \neq 0$ for all $\rho \in [0, R]$,*
3. *The function*

$$G_n(\rho) = \frac{\partial}{\partial \rho} \int_0^\rho \frac{g_n(s)}{(\rho - s)^{1/2}} ds$$

is continuous for $\rho \in [0, R]$.

Under the assumptions of the theorem and using the method of kernel transformation [40, §50], one can transform Volterra equation of the first kind to Volterra equation of the second kind which has a unique solution (see [40, §3]). This derivation was used in the results of [5,6] to provide analytical inversion formulas for a class of circular and elliptical Radon transforms with radially partial data. Such an exact inversion formula, as it turns out, is numerically unstable. Therefore, we approach the numerical inversion problem by solving (13) directly. We use the so-called trapezoidal product integration method proposed in [41]; see also [33]. For the sake of completeness, we briefly sketch this method below.

Rewrite (13) as

$$\tilde{g}_n(\rho) = \int_0^\rho \frac{k_n(\rho, u)}{\sqrt{\rho-u}} F_n(u) du \quad (14)$$

where

$$k_n(\rho, u) = \frac{K_n(\rho, u)}{K_n(\rho, \rho)}, \quad \tilde{g}_n(\rho) = \frac{g_n(\rho)}{K_n(\rho, \rho)}.$$

Let M be a positive even integer and $\rho_l = lh, l = 0, \dots, M$ and $h = \frac{R-\epsilon}{M}$ be a discretization of $[0, R - \epsilon]$. From (14) we have

$$\tilde{g}_n(\rho_i) = \sum_{k=1}^i \int_{\rho_{k-1}}^{\rho_k} \frac{k_n(\rho_i, u)}{\sqrt{\rho_i-u}} F_n(u) du$$

In the sub-interval $[\rho_{k-1}, \rho_k]$, we approximate $F_n(u)k_n(\rho_i, u)$ by a linear function taking the values $F_n(\rho_{k-1})k_n(\rho_i, \rho_{k-1})$ and $F_n(\rho_k)k_n(\rho_i, \rho_k)$ at the end-points ρ_{k-1} and ρ_k , respectively. This is given by

$$F_n(u) k_n(\rho_i, u) \approx F_{k-1}^n (k_n(\rho_i, \rho_{k-1}) \frac{\rho_k - u}{h} + F_k^n k_n(\rho_i, \rho_k) \frac{u - \rho_{k-1}}{h}).$$

Hence

$$\tilde{g}_n(\rho_i) \approx \sum_{k=1}^i \int_{\rho_{k-1}}^{\rho_k} \frac{1}{\sqrt{\rho_i-u}} \{F_{k-1}^n k_n(\rho_i, \rho_{k-1}) \frac{\rho_k - u}{h} + F_k^n k_n(\rho_i, \rho_k) \frac{u - \rho_{k-1}}{h}\} du.$$

A straightforward computation gives

$$\int_{\rho_{k-1}}^{\rho_k} \frac{\rho_k - u}{\sqrt{\rho_i-u}} du = -\frac{4}{3} h^{3/2} \left\{ (i-k+1)^{3/2} - (i-k)^{3/2} + 2(i-k+1)^{1/2} \right\}.$$

In a similar way

$$\int_{\rho_{k-1}}^{\rho_k} \frac{u - \rho_{k-1}}{\sqrt{\rho_i-u}} du = \frac{4}{3} h^{3/2} \left\{ (i-k+1)^{3/2} - (i-k)^{3/2} - 2(i-k)^{1/2} \right\}.$$

Hence

$$\begin{aligned} \tilde{g}_n(\rho_i) = & \sqrt{h} \sum_{k=1}^i \left(-\frac{4}{3} \{ (i-k+1)^{3/2} - (i-k)^{3/2} \} + 2(i-k+1)^{1/2} \right) \\ & \times F_n(\rho_{k-1}) k_n(\rho_i, \rho_{k-1}) + \\ & \left(\frac{4}{3} \{ (i-k+1)^{3/2} - (i-k)^{3/2} \} - 2(i-k)^{1/2} \right) \\ & \times F_n(\rho_k) k_n(\rho_i, \rho_k). \end{aligned} \quad (15)$$

Recall that $F_n(R-t) = f_n(t)$ and because of the assumptions on the support of f , we have that $F_n(0) = 0$ for all n . Then (15) reduces to

$$\sqrt{h} \left\{ \sum_{k=1}^i a_{i-k} k_n(\rho_i, \rho_k) F_n(\rho_k) \right\} = \tilde{g}_n(\rho_i), \quad i = 1, \dots, M \quad (16)$$

where

$$a_0 = \frac{4}{3}, \quad a_i = \frac{4}{3} \{ (i+1)^{3/2} - 2i^{3/2} + (i-1)^{3/2} \}, \quad i = 1, \dots, M.$$

The following theorem states the error estimate for the solution of the integral equation.

Theorem 5 (Error Estimates) [41, Thm. 4.1] *Let F_n^{exact} be the C^3 solution of (14) in $[0, R - \varepsilon]$ and F_n be the solution to (16). Then*

$$\max_{0 \leq i \leq M} \|F_n^{\text{exact}}(\rho_i) - F_n(\rho_i)\| = \mathcal{O}(h^2). \quad (17)$$

Equation (16) can be written in matrix form as

$$A_n F_n = \tilde{g}_n, \quad (18)$$

where

$$F_n = \begin{pmatrix} F_n(\rho_1) \\ \vdots \\ F_n(\rho_M) \end{pmatrix}, \quad \tilde{g}_n = \begin{pmatrix} \tilde{g}_n(\rho_1) \\ \vdots \\ \tilde{g}_n(\rho_M) \end{pmatrix} \quad (19)$$

and

$$A_n(i, k) = \begin{cases} a_{i-k} \sqrt{h} k_n(\rho_i, \rho_k) & 1 \leq k \leq i \\ 0 & k > i. \end{cases} \quad (20)$$

Equation (18) has a unique solution because the eigenvalues of the matrix A_n are $\frac{4}{3}\sqrt{h} > 0$. Figure 2 shows the condition number of A_n for different values of n . Since A_n is ill-conditioned for several values of n we use the Truncated Singular Value Decomposition (TSVD) [21] to solve (18).

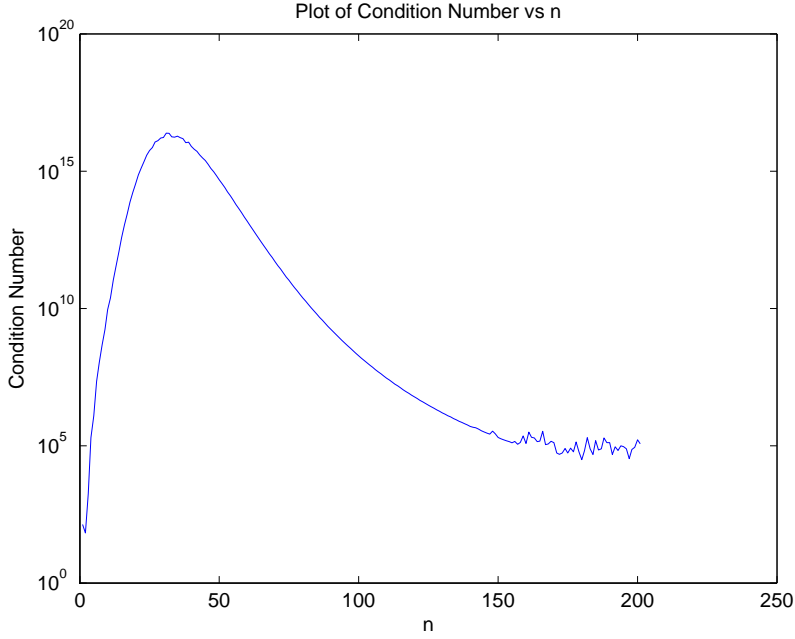


Fig. 2: Plot of condition number of A_n for $n \in [1, 200]$

3.3 Truncated singular value decomposition (TSVD)

In order to solve (18), we begin with the SVD of A_n . This is given by $A_n = UDV^T$, where U and V are orthogonal matrices whose columns are the eigenvectors of $A_n A_n^T$ and $A_n^T A_n$ respectively and D is a diagonal matrix consisting of the singular values of A , that is, the square root of the eigenvalues of $A_n^T A_n$ in descending order represented by σ_i , $i = 1, \dots, M$. Now we set

$$A_{n,r} = U D_r V^T \quad \text{and} \quad A_{n,r}^{-1} = V D_r^{-1} U^T$$

where D_r and D_r^{-1} are diagonal matrices with diagonal entries

$$(D_r)_{ii} = \begin{cases} D_{ii} & \text{if } i \leq r \\ 0 & \text{otherwise.} \end{cases} \quad (D_r^{-1})_{ii} = \begin{cases} \frac{1}{D_{ii}} & \text{if } i \leq r \\ 0 & \text{otherwise.} \end{cases}$$

The matrix $A_{n,r}$ approximates A_n , where $1 \leq r \leq M$ is the rank of the matrix $A_{n,r}$, as follows.

Let us define the 2-norm of a matrix A by

$$\|A\|_2 = \sup_{x \neq 0} \frac{\|Ax\|_2}{\|x\|_2}. \quad (21)$$

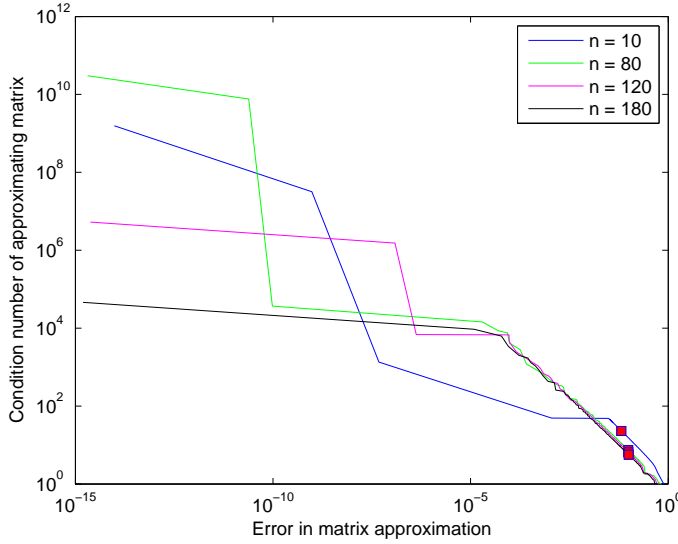


Fig. 3: Relation between condition number of $A_{n,r}$ and the error in 2-norm from the original matrix A_n , respectively for $n = 10, 80, 120, 180$. The dots on the figures correspond to the half-rank approximation.

It is well known that $\|A\|_2$ is the largest singular value of A [22]. We have that the condition number $\kappa(A_{n,r})$ of $A_{n,r}$ is given by $\kappa(A_{n,r}) = \frac{\sigma_1}{\sigma_r}$ [21].

Furthermore $\|A_n - A_{n,r}\|_2 = \sigma_{r+1}$. Therefore $A_{n,r}$ for r large, would be a good approximation to A_n , but with high condition number, whereas if r is small, the condition number would be small but the error in the approximation $\|A - A_{n,r}\|_2$ would be large.

Figure 3 shows the relation between the condition number of the truncated matrix $A_{n,r}$ and the error $\|A_n - A_{n,r}\|_2$, where the norm is defined by (21), for the Fourier coefficients $n = 10, 80, 120$ and 180 . For simplicity we considered the matrix arising out of the integral equation (1). The other cases are similar.

Due to the competing considerations mentioned above, in all our reconstructions, we chose half-rank approximations ($r = M/2$, where recall that M is the number of discretizations in ρ) to A_n for all n . The condition number of the approximating matrix $A_{n,M/2}$ in all the cases was found to be less than 10. Note that our choice of approximation was independent of the Radon data. Half-rank approximations gave good reconstructions for both the circular and elliptical Radon transforms considered here; see §4. We also tested the scheme with rank approximations $r \gg \frac{M}{2}$ and $r \ll \frac{M}{2}$ and found the results to be worse compared to the half-rank approximation case. See Figures 6a and 6b in §4.

3.4 Numerical solution of Volterra-type integral equation of second kind

The method of the previous section can also be applied to Volterra-type integral equations of the second kind. It again leads to a non-singular matrix A_n with high condition number.

Given a Volterra integral equation of the first kind,

$$g_n(\rho) = \int_0^\rho \frac{K_n(\rho, u)F_n(u)}{\sqrt{\rho - u}} du,$$

one can transform this into a Volterra-type integral equation of the second kind [40] which is given by

$$G_n(\rho) = F_n(\rho) + \int_0^\rho L_n(\rho, u)F_n(u)du \quad (22)$$

where

$$G_n(\rho) = \frac{1}{\pi K_n(t, t)} \frac{d}{d\rho} \int_0^\rho \frac{g_n(u)}{\sqrt{\rho - u}} du$$

and

$$L_n(\rho, u) = \frac{1}{\pi K_n(\rho, \rho)} \frac{d}{d\rho} \int_u^\rho \frac{K_n(t, u)}{\sqrt{t - u}\sqrt{\rho - t}} dt.$$

We can apply the trapezoidal product integration method to (22) with the discretization $\rho_l = lh$, $l = 0, \dots, M$ and $h = \frac{R-\epsilon}{M}$ of $[0, R - \epsilon]$ and we arrive at the following matrix equation:

$$(I + A_n)F_n = G_n \quad (23)$$

where F_n and G_n are similar to (19) and

$$A_n(i, k) = \begin{cases} a_k L_n(\rho_i, \rho_k) & 1 \leq k \leq i \\ 0 & j > i \end{cases} \quad (24)$$

with $a_k = h$, for $k = 1 \dots i - 1$ and $a_i = h/2$.

Remark 1 One could apply the numerical algorithm given in this paper to the matrix equation (24). However, the evaluation of G_n and L_n involves calculating derivative of an integral which leads to numerical instabilities and hence a high percentage of error. Furthermore, numerical computation of G_n and L_n is time consuming.

4 Numerical Results

We now show the results of the numerical computations performed for the circular and elliptical Radon transforms considered in Theorems 1, 2 and 3. The trapezoidal integration method requires the function to be recovered to be C^3 for $\mathcal{O}(h^2)$ convergence of the approximate solution to the actual one (see Theorem 5). Nevertheless, we tested our algorithm on functions with jump singularities and it gave good reconstructions. We discretized $\phi \in [0, 2\pi]$ into 400 equally spaced grid points and $\rho \in [0, R - \varepsilon]$ (we chose $\varepsilon = 0.0024$) into 400 equally spaced grid points for all the computations. Additionally, we tested the numerical algorithm on 1000 equally spaced grid points in the ρ space for the computations in §4.1.1 and §4.1.2. In all cases we take $R = 1$ unless mentioned otherwise. Besides analyzing the physical properties of the reconstructed image, we also evaluate the relative L^2 error percentage between the actual and the reconstructed images, which is defined as

$$\text{Relative } L^2 \text{ error percentage} = \frac{\|f_{\text{rec}} - f_{\text{ex}}\|}{\|f_{\text{ex}}\|} * 100\%$$

where $f_{\text{ex}} = f_{\text{ex}}(x_i, y_j)$ and $f_{\text{rec}} = f_{\text{rec}}(x_i, y_j)$, $i, j = 1 \dots M$ represents the discretized matrix for the exact function and the reconstructed function respectively, $\|f\| = \frac{1}{M} \sqrt{\sum_{i=1}^M \sum_{j=1}^M f_{ij}^2}$ and $f = f(x_i, y_j)$.

4.1 Functions supported in an interior annulus

This corresponds to the case when the object we are interested in reconstructing is supported in an annulus centered at 0 of the circle $\partial B(0, R)$ and the circular and elliptical Radon transforms are along circles (ellipses) with center (foci) on $\partial B(0, R)$, see Theorem 1. For the circular Radon transform case, the matrix A_n consists of entries coming from the kernel equation (2), whereas for the elliptical Radon transform case, the matrix entries come from (4).

In both the circular and elliptic transform cases discussed below, we notice a good recovery of the image near the origin which is a point of singularity. There is reduction in the number of artifacts as we increase the number of discretization points and hence the relative L^2 error decreases with increasing refinement.

4.1.1 Circular Radon transform data

Figure 4a shows the Shepp-Logan phantom which is recovered by numerical inversion in Figures 4b, 4c and 4d using 400 (without and with 10 % Gaussian noise) and 1000 equally spaced discretizations in ρ , respectively. The relative L^2 errors between Figures 4a and 4b, Figures 4a and 4c, and Figures 4a and 4d are 18.6%, 24.2% and 10.1%, respectively. A smooth version of the Shepp-Logan phantom is shown in Figure 5 which is also recovered well by the

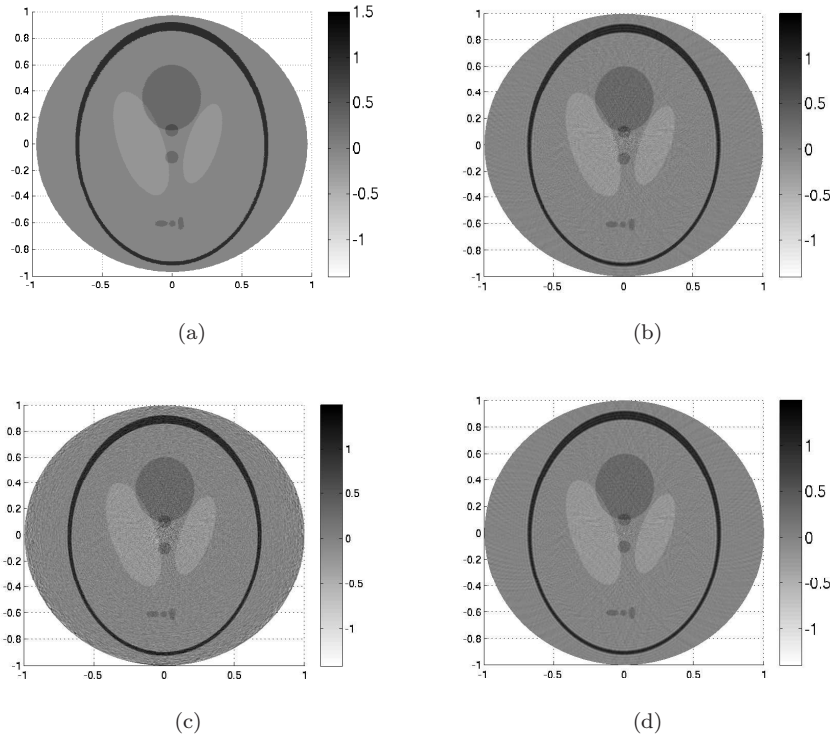


Fig. 4: Results for circular Radon transform data for a function supported in an interior annulus of $\partial B(0, R)$. Figure 4a shows the actual Shepp-Logan phantom and Figures 4b, 4c and 4d show the reconstructed images with 400, 400 with 10% added Gaussian noise, and 1000 equally spaced discretizations in ρ , respectively.

inversion formula. The relative L^2 error between these images is 5.7%, showing that the algorithm performs better with smooth initial data.

To justify the rationale behind half-rank approximations, we tested the algorithm with rank approximations $r = M/8$ and $r = M/1.5$. The results are shown in Figures 6a and 6b respectively. The relative L^2 error for the first case was 65.8% and for the second case was 280.1%. This suggests rank approximations too far away from half-rank approximations can either lead to loss of data or lead to blow-offs which results in improper reconstruction.

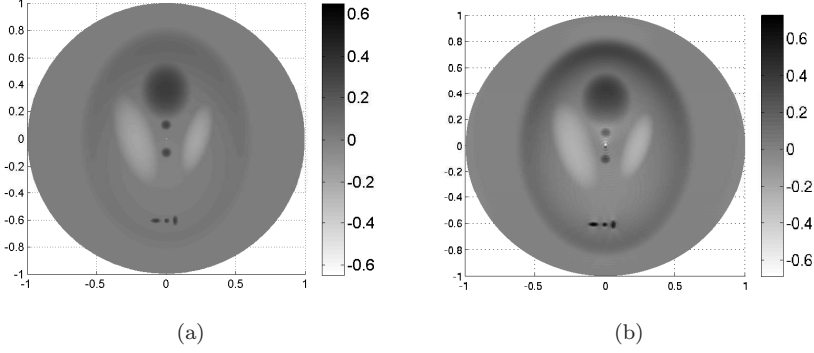


Fig. 5: Results for circular Radon transform data for a function supported in an interior annulus of $\partial B(0, R)$. Figure 5a shows a smooth version of the Shepp-Logan phantom and Figure 5b shows the reconstructed image.

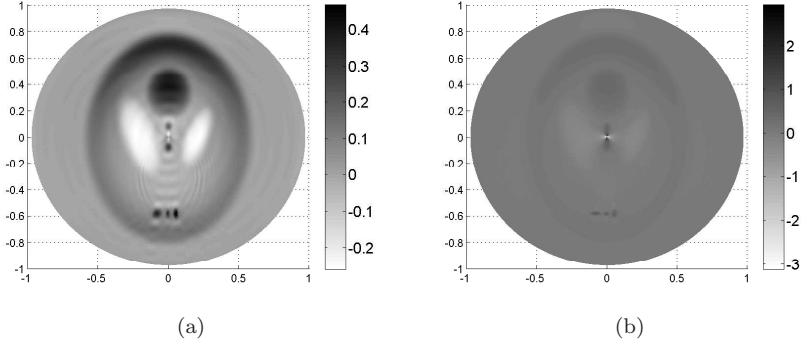
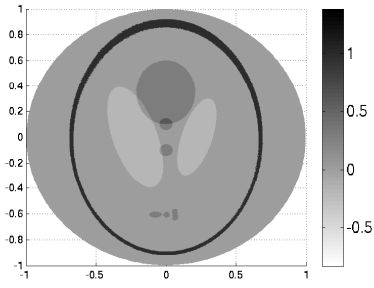


Fig. 6: Results for circular Radon transform data for a function supported in an interior annulus of $\partial B(0, R)$. Figure 6a shows the reconstruction of smooth version of the Shepp-Logan phantom with $r = M/8$ and Figure 6b shows the reconstruction with $r = M/1.5$. Figure 6a reveals incomplete reconstruction due to loss of data whereas Figure 6b reveals blow-off in the solution.

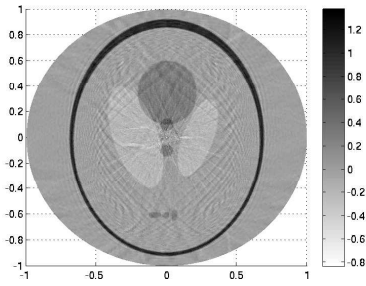
4.1.2 Elliptical Radon transform data

Figure 7 shows the actual and reconstructed images with 400 and 1000 equally spaced discretizations in ρ from elliptical Radon transform data using the numerical algorithm of Section 3 based on the result of Part 2 of Theorem 1.

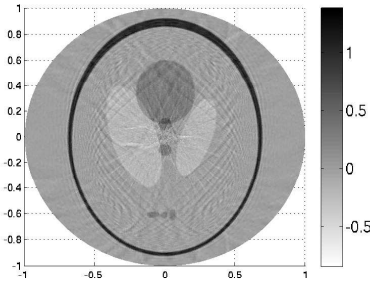
For the computations we assumed that an object is placed inside the annulus $A(\epsilon, b)$ where $b = R \cos \alpha$ with $\alpha = 30^\circ$ is the length of the semi-minor axis. The resulting integral equation to be solved is given by (3) with the kernel $K_n(\rho, u)$ given by (4). We see that all the objects in the image have been



(a)



(b)



(c)

Fig. 7: Results of elliptical Radon transform data for a function supported in an interior annulus of $\partial B(0, R)$. Figure 7a shows the actual Shepp-Logan phantom and Figures 7b and 7c show the reconstructed images with 400 and 1000 equally spaced discretizations in ρ , respectively.

reconstructed even with the coarser discretization of 400 points. The relative L^2 errors between the Figures 7a and 7b, and between the Figures 7a and 7c are 14.2% and 10.6%, respectively.

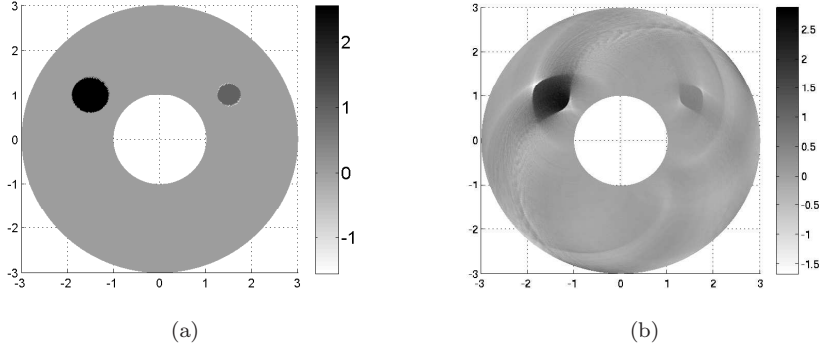


Fig. 8: Results for circular Radon transform data for a function supported in an annular region of $C(R, 3R)$. The circular Radon transform data is taken over circles centered on the inner circle. Figure 8b shows the reconstructed image.

4.2 Functions supported inside $A(R, 3R)$

In this test case, we use circular Radon transform data for functions supported inside $A(R, 3R)$. The integral equation to be considered in this case is (6) with the kernel $K_n(\rho, u)$ as defined in (7). The actual and reconstructed images are shown in Figure 8. Microlocal analysis arguments show that the entire circumference of the two circles cannot be constructed stably with the given circular Radon transform data [19, 20, 18, 35]. We see the presence of an increased number of artifacts in contrast to the interior case (see §4.1.1). The image reconstructed is consistent with this analysis. The relative L^2 error between these images is 35.5%. While the error is large, the number and location of the objects in the image are recovered.

4.3 Functions supported on both sides of $\partial B(0, R)$

4.3.1 Circular Radon transform data for functions supported on both sides of $\partial B(0, R)$

We considered a function supported inside the annulus $A(R_1, R_2)$ where $R_2 > 2R$ and $R_1 = R_2 - 2R$ (See Figure 9a). In the computations we chose $R = 1.47$, $R_2 = 3$. Therefore $R_1 = 0.06$. The resulting integral equation is given by (8) with the kernel $K_n(\rho, u)$ defined by (9). The actual and reconstructed images are shown in Figure 9. As in Figure 8, microlocal analysis of the given circular Radon transform data shows that certain parts of boundary of the disc outside the dotted circle cannot be stably reconstructed. Note that the

boundary of inner disc is reconstructed well. The relative L^2 error between these images is 32.1%.

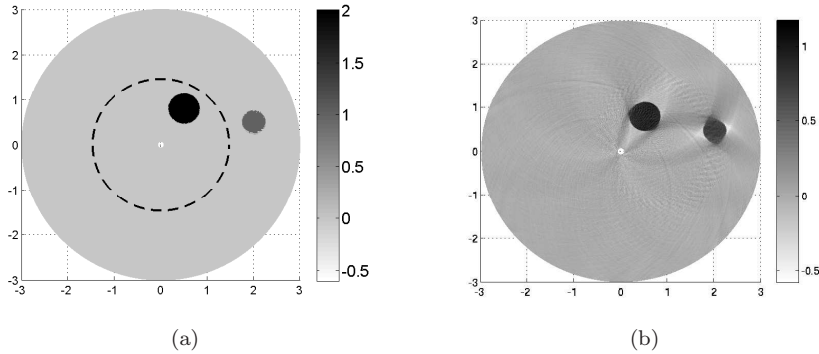


Fig. 9: Simulation with circular Radon transform data (Part 1 of Thm 3) for a function supported on both sides of the circle $\partial B(0, R)$ shown by the dotted circle in Figure 9a. Figure 9a shows the actual image and Figure 9b shows the reconstructed image.

4.3.2 Elliptical Radon transform data for functions supported on both sides of $\partial B(0, R)$

Finally, we tested our algorithm for Part 2 of Theorem 3. We considered a function placed inside the annulus $A(R_1, R_2)$ where we chose the angle $\alpha = 20^\circ$, $R = 1.47$ and $R_2 = 3$. Then $R_1 = R_2 - 2b = R_2 - 2R \cos 20^\circ \approx 0.237$. We tested the numerical algorithm on the integral equation (10) with the kernel $K_n(\rho, u)$ given by (11) and the results are shown in Figure 10. Same microlocal analysis reasons [3] as in Figure 9 applies for this case as well. The relative L^2 error between these images is 31.8% without noise and with 10% Gaussian noise, the relative L^2 error is 52.2%.

5 Summary

We have developed a numerical technique to solve the inversion formulas for circular and elliptical Radon transforms arising in some imaging applications. The inversion formulae and the proposed numerical scheme have been demonstrated to give good reconstructions on some standard test problems involving both discontinuous and smooth images. While the absolute errors in the reconstructed image are large, especially for discontinuous images, what is

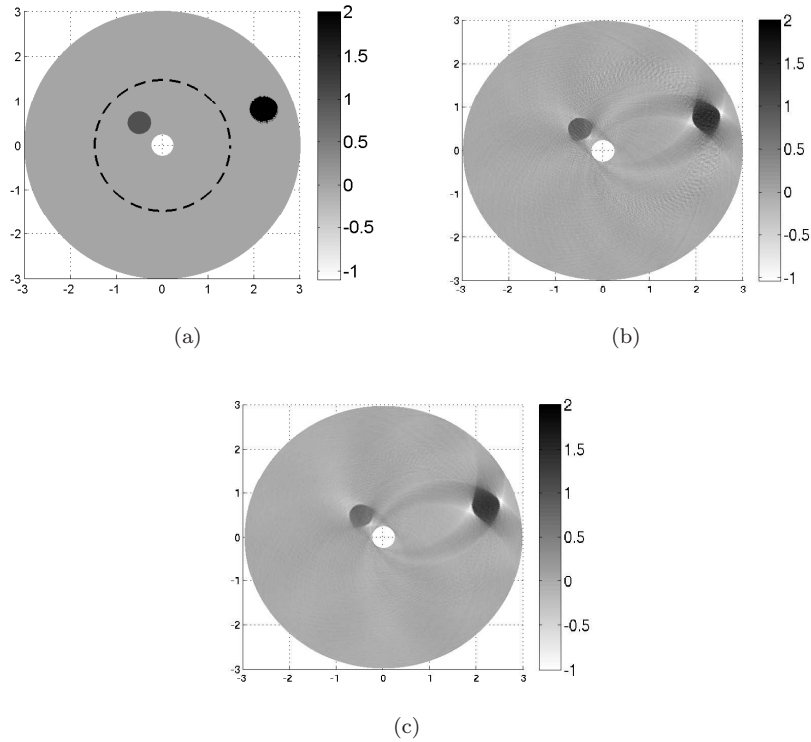


Fig. 10: Simulation with elliptical Radon transform data (Part 2 of Theorem 3) for a function supported on both sides of the circle $\partial B(0, R)$ shown by the dotted circle in Figure 10a. Figure 10a shows the actual image, Figure 10b and Figure 10c show the reconstructed image without and with 10% Gaussian noise, respectively.

more important is that the objects in the image are property distinguished by the current method. The numerical algorithm requires the solution of ill-conditioned matrix problems which is accomplished using a truncated SVD method. The matrices and the SVD can be constructed in a pre-processing step and re-used repeatedly for the subsequent computations leading to an efficient and fast algorithm.

Acknowledgments

VPK would like to thank Rishu Saxena for her valuable input and discussions during the initial stages of this work. SR and VPK would like to express their gratitude to Gaik Ambartsoumian and Eric Todd Quinto for several fruitful discussions and important suggestions.

VPK was partially supported by NSF grant DMS 1109417. All authors benefited from the support of the AIRBUS Group Corporate Foundation Chair “Mathematics of Complex Systems” established at TIFR Centre for Applicable Mathematics and TIFR International Centre for Theoretical Sciences, Bangalore, India.

References

1. Mark Agranovsky, Carlos Berenstein, and Peter Kuchment. Approximation by spherical waves in L^p -spaces. *J. Geom. Anal.*, 6(3):365–383 (1997), 1996.
2. Mark Agranovsky and Eric Todd Quinto. Injectivity sets for Radon transform over circles and complete systems of radial functions. *J. Functional Anal.*, 139:383–414, 1996.
3. Gaik Ambartsoumian, Jan Boman, Venkateswaran P. Krishnan, and Eric Todd Quinto. Microlocal analysis of an ultrasound transform with circular source and receiver trajectories. American Mathematical Society, series =Contemporary Mathematics, volume =598, pages =45 – 58, 2013.
4. Gaik Ambartsoumian, Raluca Felea, Venkateswaran P. Krishnan, Clifford Nolan, and Eric Todd Quinto. A class of singular Fourier integral operators in synthetic aperture radar imaging. *J. Funct. Anal.*, 264(1):246–269, 2013.
5. Gaik Ambartsoumian, Rim Gouia-Zarrad, and Matthew A. Lewis. Inversion of the circular Radon transform on an annulus. *Inverse Problems*, 26(10):105015, 11, 2010.
6. Gaik Ambartsoumian and Venkateswaran P. Krishnan. Inversion of a class of circular and elliptical Radon transforms. 2014. To appear in Contemporary Mathematics, Proceedings of the international conference on Complex Analysis and Dynamical Systems VI, 2013.
7. Gaik Ambartsoumian and Peter Kuchment. On the injectivity of the circular Radon transform. *Inverse Problems*, 21(2):473–485, 2005.
8. Gaik Ambartsoumian and Leonid Kunyansky. Exterior/interior problem for the circular means transform with applications to intravascular imaging. *Inverse Probl. Imaging*, 8(2):339–359, 2014.
9. Lars-Erik Andersson. On the determination of a function from spherical averages. *SIAM J. Math. Anal.*, 19(1):214–232, 1988.
10. Yuri A. Antipov, Ricardo Estrada, and Boris Rubin. Method of analytic continuation for the inverse spherical mean transform in constant curvature spaces. *J. Anal. Math.*, 118(2):623–656, 2012.
11. Allen M. Cormack. Representation of a function by its line integrals, with some radiological applications. *J. Appl. Phys*, 34(9):2722 – 2727, 1963.
12. Alexander Denisjuk. Integral geometry on the family of semi-spheres. *Fract. Calc. Appl. Anal.*, 2(1):31–46, 1999.
13. John A. Fawcett. Inversion of n -dimensional spherical averages. *SIAM J. Appl. Math.*, 45(2):336–341, 1985.
14. David Finch, Markus Haltmeier, and Rakesh. Inversion of spherical means and the wave equation in even dimensions. *SIAM J. Appl. Math.*, 68(2):392–412, 2007.
15. David Finch, Sarah K. Patch, and Rakesh. Determining a function from its mean values over a family of spheres. *SIAM J. Math. Anal.*, 35(5):1213–1240 (electronic), 2004.
16. David Finch and Rakesh. The spherical mean value operator with centers on a sphere. *Inverse Problems*, 23(6):S37–S49, 2007.
17. Jürgen Frikel and Eric Todd Quinto. Artifacts in incomplete data tomography with applications to photoacoustic tomography and sonar. 2014. Preprint.
18. Allan Greenleaf and Gunther Uhlmann. Non-local inversion formulas for the X-ray transform. *Duke Math. J.*, 58:205–240, 1989.
19. Victor Guillemin. Some remarks on integral geometry. Technical report, MIT, 1975.
20. Victor Guillemin and Shlomo Sternberg. *Geometric asymptotics*. American Mathematical Society, Providence, R.I., 1977. Mathematical Surveys, No. 14.

21. Per Christian Hansen. The truncated SVD as a method for regularization. *BIT*, 27(4):534–553, 1987.
22. Roger A. Horn and Charles R. Johnson. *Matrix analysis*. Cambridge University Press, Cambridge, second edition, 2013.
23. Peter Kuchment and Leonid Kunyansky. Mathematics of thermoacoustic tomography. *European J. Appl. Math.*, 19(2):191–224, 2008.
24. M. M. Lavrentiev, V. G. Romanov, and V. G. Vasiliev. *Multidimensional inverse problems for differential equations*. Lecture Notes in Mathematics, Vol. 167. Springer-Verlag, Berlin-New York, 1970.
25. Serge Mensah and Émilie Franceschini. Near-field ultrasound tomography. *J. Acoust. Soc. Am*, 121.
26. Serge Mensah, Émilie Franceschini, and Jean-Pierre Lefevre. Mammographie ultrasonore en champ proche. *Trait. Signal*, 23(3-4):259–276, 2006.
27. Serge Mensah, Émilie Franceschini, and Marie-Christine Pausin. Ultrasound mammography. *Nuclear Instruments and Methods in Physics Research*, 571(3):52–55, 2007.
28. Sunghwan Moon. On the determination of a function from an elliptical Radon transform. *J. Math. Anal. Appl.*, 416(2):724–734, 2014.
29. Linh V. Nguyen. A family of inversion formulas in thermoacoustic tomography. *Inverse Probl. Imaging*, 3(4):649–675, 2009.
30. Linh V. Nguyen. Spherical mean transform: a PDE approach. *Inverse Probl. Imaging*, 7(1):243–252, 2013.
31. Stephen J. Norton. Reconstruction of a two-dimensional reflecting medium over a circular domain: exact solution. *J. Acoust. Soc. Amer.*, 67(4):1266–1273, 1980.
32. Stephen J. Norton and Melvin Linzer. Reconstructing spatially incoherent random sources in the nearfield: exact inversion formulas for circular and spherical arrays. *J. Acoust. Soc. Amer.*, 76(6):1731–1736, 1984.
33. Robert Plato. The regularizing properties of the composite trapezoidal method for weakly singular Volterra integral equations of the first kind. *Adv. Comput. Math.*, 36(2):331–351, 2012.
34. William H. Press, Saul A. Teukolsky, William T. Vetterling, and Brian P. Flannery. *Numerical recipes in C*. Cambridge University Press, Cambridge, second edition, 1992. The art of scientific computing.
35. Eric Todd Quinto. Singularities of the X-ray transform and limited data tomography in \mathbb{R}^2 and \mathbb{R}^3 . *SIAM J. Math. Anal.*, 24:1215–1225, 1993.
36. V. G. Romanov. An inversion formula in a problem of integral geometry on ellipsoids. *Mat. Zametki*, 46(4):124–126, 1989.
37. Boris Rubin. Inversion formulae for the spherical mean in odd dimensions and the Euler-Poisson-Darboux equation. *Inverse Problems*, 24(2):025021, 10, 2008.
38. F. G. Tricomi. *Integral equations*. Dover Publications, Inc., New York, 1985. Reprint of the 1957 original.
39. V. V. Volchkov. *Integral geometry and convolution equations*. Kluwer Academic Publishers, Dordrecht, 2003.
40. Vito Volterra. *Theory of functionals and of integral and integro-differential equations*. With a preface by G. C. Evans, a biography of Vito Volterra and a bibliography of his published works by E. Whittaker. Dover Publications, Inc., New York, 1959.
41. Richard Weiss. Product integration for the generalized Abel equation. *Math. Comp.*, 26:177–190, 1972.